Research Article

Role of Bi^{3+} ions on structural, optical, photoluminescence and electrical performance of $Cd_{0.9-x}Zn_{0.1}Bi_xS$ QDs

A. Krishnamoorthy[1] · P. Sakthivel[2] · I. Devadoss[1] · V. M. Anitha Rajathi[3]

Received: 23 September 2020 / Accepted: 1 June 2021
Published online: 10 June 2021

Abstract
In this work, the $Cd_{0.9-x}Zn_{0.1}Bi_xS$ QDs with different compositions of Bi^{3+} ions ($0 \le x \le 0.05$) were synthesized using a facile chemical route. The prepared QDs were characterized for analyzing the structural, morphological, elemental, optical, band gap, photoluminescence and electrochemical properties. XRD results confirmed that the $Cd_{0.9-x}Zn_{0.1}Bi_xS$ QDs have a cubic structure. The mean crystallite size was increased from ~ 2 to ~ 5 nm for the increase of Bi^{3+} ions concentration. The optical transmittance behavior was decreased with increasing Bi^{3+} ions. The scanning electron microscope images showed that the prepared QDs possessed agglomerated morphology and the EDAX confirmed the presence of doped elements as per stoichiometry ratio. The optical band gap was slightly blue-shifted for initial substitution (Bi^{3+} = 1%) of Bi^{3+} ions and red-shifted for further increase of Bi^{3+} compositions. The optical band gap was ranged between 3.76 and 4.0 eV. High intense red emission was received for Bi^{3+} (1%) doped Zn:CdS QDs. The red emission peaks were shifted to a higher wavelength side due to the addition of Bi^{3+} ions. The PL emission on UV-region was raised for Bi^{3+} (1%) and it was diminished. Further, a violet (422 nm) and blue (460 nm) emission were received for Bi^{3+} ions doping. The cyclic voltammetry analysis showed that Bi^{3+} (0%) possessed better electrical properties than other compositions of Bi^{3+} ions.

Keywords Bi^{3+} · CdS · Photoluminescence · Blue shift · Electrochemical

1 Introduction

The Quantum dots (QDs) consist of semiconductor nanoparticles which dimension varies from 1 to 10 nm [1–3]. The combination of (III–V) and (II–VI) semiconductors is getting significant than the IV semiconductors. QDs are more photo-stable, higher signal-to-noise ratio, sharp and narrow emission spectra, longer fluorescence and higher photo-resistance compare to conventional organic dyes. These unique properties of QDs are attracted much attention in the field of biomedical imaging and optoelectronic devices like sensors, photoconductive cells, photovoltaic cells and solar cells, etc. Quantum dots play a substantial role in the imaging and labeling techniques, especially CdS, ZnSe, ZnS are having much significance [4]. CdS QDs based fluorescence sensors find novel application in modern technology [5]. In particular, the fluorescence emission wavelength from deep red (DR) to near-infrared (NIR) region is highly required for bio-imaging sensor designing and other bio-medical applications. Self-induced fluorescence interference, reduced light scattering, a high degree of penetration depth and less tissue damage are the important aspects due to the minimized emission

✉ P. Sakthivel, sakthi1807@gmail.com | [1]PG & Research Department of Physics, Bishop Heber College (Affiliated to Bharathidasan University), Tamil Nadu, Tiruchirappalli 620 017, India. [2]Department of Physics, Centre for Materials Science, Faculty of Engineering, Karpagam Academy of Higher Education, Tamil Nadu, Coimbatore 641 021, India. [3]Department of Management Studies, UCE-BIT Campus, Anna University, Tamil Nadu, Tiruchirappalli 620 024, India.

bands**.** The DR and NIR region may be achieved by the various combination of QDs [6–8].

For the past two decades, CdS and ZnS series elements have been widely used to develop optical, optoelectronic device applications. CdS find a distinct advantage on luminescent and optoelectronic applications [9]. Cd-Zn–S QDs need some advantage since fast recombination of charge carriers. But these materials are having good efficiency for photolysis depends on the integration with appropriate dopants like Ni, Bi, Ba, Sb, Mn, Co, Fe, etc. Among these transition metals, bismuth is a good candidate to enhance the optical, electrical and magnetic properties (ZnBiS, Bi:CdS, Bi:CdZnS, Bi_2O_3, BiOCl, $BiVO_4$, Bi_2WO_6, and Bi_2MoO_6) [10–13]. We have already reported the structural, morphological and photoluminescence properties of $Cd_{0.8}Zn_{0.2}S$ nanomaterials with the influence of Fe^{2+} ions. It was noticed that the PL spectra were blue-shifted for the increase of Fe^{2+} concentrations. At the higher wavelength ($\lambda \sim 650$ nm) side the band emission (DLE) move towards the redshift. It is required that a higher fluorescence emission band ($\lambda > 650$ nm) for biomedical and other deep red band emission applications, these may overcome by using bismuth materials [14]. So far few reports have been published on bismuth-doped Cd-Zn–S QDs for optical property activity exploration. There are many kinds of synthesis that were carried out to get CdS nanoparticles like sol–gel, hydrothermal, solvothermal, microwave-assisted method, sonochemical and co-precipitation method [15–17]. The co-precipitation method is identified as a simple and cost-effective method to synthesize nanoparticles in Mass quantity [18]. Hence we have selected the co-precipitation method for the preparation of the proposed combination of CdS nanoparticles. The present investigation deals with the synthesis of bismuth-doped cadmium-zinc-sulfide QDs ($Cd_{0.9-x}Zn_{0.1}Bi_xS$ QDs, where x = 0, 0.01, 0.03 and 0.05) using the co-precipitation method.

2 Experimental details

2.1 Materials used

The QDs of $Cd_{0.9}Zn_{0.1}S$ doped with the various compositions of Bi^{3+} ions have been synthesized by the facile chemical route. The cadmium acetate dihydrate [$Cd(CH_3COOH)_2{\cdot}2H_2O$], bismuth acetate dihydrate [$Bi(C_2H_3O_2)_3$], zinc acetate dihydrate [$Zn(CH_3COO)_2.2H_2O$], and sodium sulfide [Na_2S] of high purity (99.9%), AR graded chemicals were used to prepare $Cd_{0.9-x}Zn_{0.1}Bi_xS$ QDs. These chemicals were purchased from M/s Merck Millipore.

2.2 Synthesis of $Cd_{0.9-x}Zn_{0.1}Bi_xS$ QDs

To synthesis Bi-doped $Cd_{0.90-x}Zn_{0.1}Bi_xS$ (x = 0,0.01,0.03,0.05) $Cd(CH_3COOH)_2{\cdot}2H_2O$) $Zn(CH_3COO)_2.2H_2O$ and $Bi(C_2H_3O_2)_3$ were taken as per stoichiometry ratio and dissolved using 50 ml DI water in a separate beaker which contains 50 ml double distilled water, respectively. These solutions were prepared under continuous stirring for 30 min. These solutions were added one by one in a beaker where on magnetic stirring. The pH value of the solution was standardized using ammonia solution and the pH value was maintained at 9. The stirring rate was 600 rpm and the duration was 4 h. Upon the successful completion of the reaction, a precipitate was obtained. In the purification process, the precipitate was filtered out, washed with deionized water and methanol to remove the impurities if any. To get nanopowders, the samples were kept in a furnace at 70 °C for 8 h for drying and properly pulverized using agar mortar to get the homogeneous fine size. The same procedure was repeated for synthesizing samples with other compositions of Bi and Cd to get $Cd_{0.9-x}Zn_{0.1}Bi_xS$ QDs (x = 0, 0.01, 0.03, 0.05).

2.3 Characterization

We have prepared the nanoparticles of $Cd_{0.9-X}Zn_{0.1}Bi_XS$ (x = 0.00, 0.01, 0.03 and 0.05) and characterized for structural, compositional, elemental, optical and electrochemical analysis of the samples. For aforesaid investigations we used X- ray diffractometer (Model: Rigaku C/max-2500) for recording the X-ray diffractions (using Cu–Kα radiation: wavelength is 1.54056 Å) from 20˚ to 80˚ with the step angle 0.02˚ per min, Scanning electron microscope (Model: JEOLJSM 6390) for Morphological and elemental analysis, FT-IR spectrometer (Model: Perkin Elmer, Make: Spectrum RXI) for molecular vibrational study, UV- spectrometer (Model: lambda 35, Make: Perkin Elmer)) for UV–vis optical absorption, transmittance, band gap analysis, PL spectrometer (Model: F-2500 Make: Hitachi) photoluminescence emission, Cyclic voltameter (Model: VersaSTAT MC electrochemical system, Make: Princeton Applied Research, USA) for CV analysis and Nyquist plot to explore the electrical properties. The studies were taken using a three-electrode cell at room temperature in the 3 wt. % NaCl solution. The niobium mesh covered with platinum was taken a role as a counter electrode. The saturated calomel electrode (SCE) was served as a reference electrode. The electrochemical impedance analysis was recorded at the constant dc potential of 0.7 V under the dark condition

from the frequency 0.1 Hz to 1 MHz with an amplitude voltage of 10 mV.

3 Result and discussions

3.1 Structural analysis

The average crystallite size (D), lattice parameter (a, b & c) micro-strain (**ε**) and crystal structure of Bi^{3+}-doped $Cd_{0.9}Zn_{0.1}S$ QDs samples were analyzed by using XRD. Figure 1 shows XRD spectrum of $Cd_{0.9-x}Zn_{0.1}Bi_xS$ QDs with different Bi^{3+} compositions ($0 \le x \le 0.05$). The observed three diffraction peaks are corresponding to the lattice planes of (111), (220) and (311) and confirmed that the $Cd_{0.9-x}Zn_{0.1}Bi_xS$ QDs possessed a cubic structure. The diffraction peaks corresponding to the cubic phase were matched with JCPDS file number 10–454 [19].

A high intense peak was observed around $2\theta = 26.80^{\circ}$ corresponding to the (111) plane for $Cd_{0.9-x}Zn_{0.1}S$ QDs. While the other samples (x = 0.01, 0.03 and 0.05) diffraction peaks were located at $2\theta = 26.6$, 26.94 and 26.65 respectively, with the same (111) plane direction. From the XRD peaks, a shift towards the lower value of 2θ and peak intensity is decreased. The shifting of 2θ is ascertained to

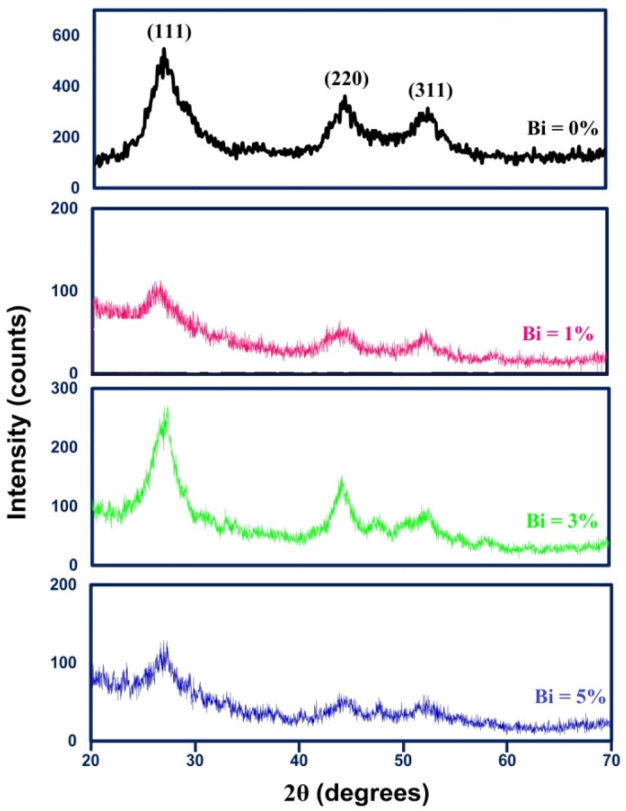

Fig. 1 XRD spectra of $Cd_{0.9-x}Zn_{0.1}Bi_xS$ QDs (x = 0,1,3 and 5 at. wt. %)

ionic radius of bismuth (Bi^{3+} = 1.03 Å) is greater than cadmium (Cd^{2+} = 0.95 Å) and Zinc (Zn^{2+} = 0.74 Å) [15]. This observation indicates that the separation of the neighboring lattice plane is longer than those of pure $Cd_{0.9-x}Zn_{0.1}S$. The variation of peak intensity concerning to Bi^{3+} doping concentration is presented in Fig. 2a.

The average crystallite size (D_{hkl}) of $Cd_{0.9}$-$xZn_{0.1}Bi_xS$ (x = 0, 0.01, 0.03, 0.05) QDs was found by using Sherrer's equation, based on the FWHM values [20].

$$D_{hkl} = \frac{k\lambda}{\beta \cos\theta} \quad (1)$$

where λ is the wavelength of X-ray diffraction, k is a constant taken to be 0.9, θ is the Bragg angle and β is denoted the full width at half maximum (FWHM) of the diffraction peak. The Table 1 reports the average crystallite size, lattice constant, FWHM, d-value, 2θ position and micro-strain value of $Cd_{0.9}$-$xZn_{0.1}Bi_xS$ (x = 0, 0.01, 0.03, 0.05) QDs. From the given data, for the increase of x-value from 0.01 to 0.05, the average crystallite size (D_{111}) was increased. It is also cleared from the decrease in the β value of XRD as shown in Table 1. [21]. The variation of XRD primary peak intensity with Bi^{3+} dopant concentration was shown in Fig. 2a. When Bi^{3+} ions doped (1%) reduced XRD peak intensity because the initial incorporation of large-sized dopant ion into the host lattice produced some distortion. The replacement of Cd^{2+} ions by Bi^{3+} ions produced defect states. Bi^{3+} (3%) doping increased the crystallinity than 1% doped nanocrystals which indicate an elevation in peak intensity. The average crystallite size is small for this concentration of Bi^{3+}. While increasing Bi^{3+} concentration to 5% reduces the peak intensity indicates the loss of crystallinity due to the distortion produced in the lattice. The creation of sulfur vacancy produced more distortion for the higher doping composition of Bi^{3+} ions. A similar decrease of peak intensity due to Bi^{3+} doping ZnO was reported in the literature [22]. While Bi^{3+} doped with ZnS nanoparticles the 2theta angle shifts lower side. the similar shift due to Bi^{3+} was reported in the literature [23]

The dislocation density (δ) is measured using the relation, $\delta = 1/D^2$. The crystal size of Cd $_{0.9-x}Zn_{0.1}Bi_xS$ QDs was increased up to 5.98 nm after Bi^{3+} doped (x = 0.05). The dislocation density was decreased by increasing the Bi^{3+} concentration as shown in Fig. 2b, which may be attributed to the increase of the crystal structure [24]. The lattice parameters of $Cd_{0.9-x}Zn_{0.1}Bi_xS$ QDs are found to lie in the range of 3.28 Å (for x = 0) to 3.34 Å (for x = 0.05). The lattice parameter of $Cd_{0.9-x}Zn_{0.1}Bi_xS$ QDs increased with the increase of Bi^{3+} ions content, which can be attributed to the replacement of Cd^{2+} shown in Fig. 2c. It was noticed that the unit cell volume ($V = a^3$) increased for Bi^{3+} doped samples, in agreement with ionic radii of Bi^{3+} (R_{Bi}) larger than ionic radii of Cd^{2+}

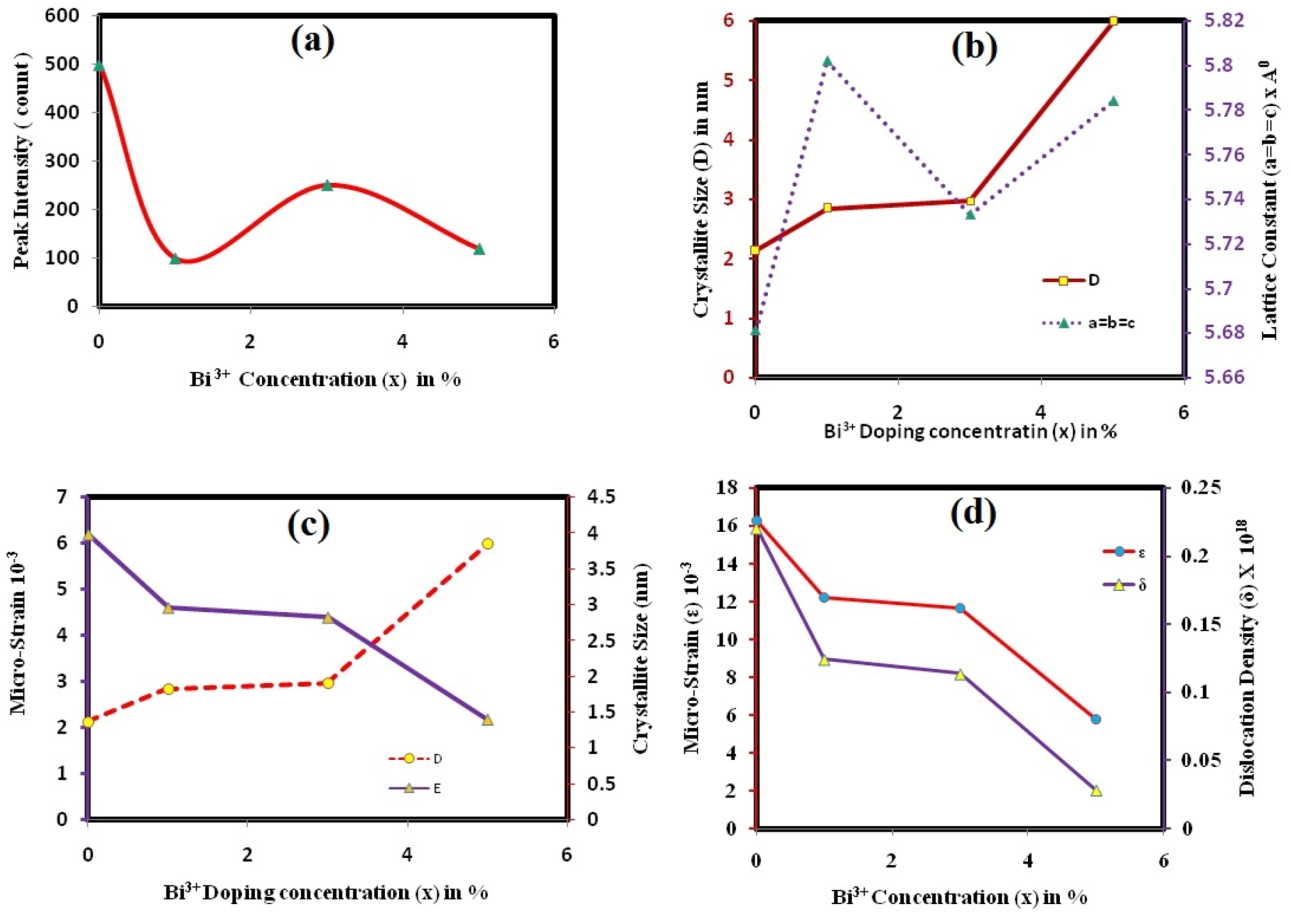

Fig. 2 **a** XRD peak intensity of $Cd_{0.9-x}Zn_{0.1}Bi_xS$ QDs (x = 0,1,3 and 5 at. wt. %), **b** $Cd_{0.9-x}Zn_{0.1}Bi_xS$ QDs 'D' and 'a' variation, **c** $Cd_{0.9-x}Zn_{0.1}Bi_xS$ QDs 'ε' and 'D' variations, **d** $Cd_{0.9-x}Zn_{0.1}Bi_xS$ QDs 'ε' and 'δ' variation

Table 1 The variation of peak position (2θ), FWHM (β) value, d-value, cell parameter 'a', average crystallite size (D) and micro-strain (ε) of $Cd_{0.9-x}Zn_{0.1}Bi_xS$ (x = 0% to 5%) nanoparticles

Samples	Peak position (2θ) (°)	FWHM (β) (°)	d-value (Å)	Lattice constant a = b = c (Å)	Average crystallite size (D) (nm)	Micro-strain(ε) (10^{-3})
$Cd_{0.9}Zn_{0.1}S$	26.80	3.98	3.280	5.681	2.13	16.281
$Cd_{0.89}Zn_{0.1}Bi_{0.01}S$	26.60	2.96	3.35	5.802	2.84	12.235
$Cd_{0.87}Zn_{0.1}Bi_{0.03}S$	26.94	2.83	3.31	5.733	2.97	11.67
$Cd_{0.85}Zn_{0.1}Bi_{0.05}S$	26.65	1.401	3.34	5.784	5.98	5.795

(R_{Cd}). This confirmed the expansion of the crystalline plane spacing due to the substitution of Bi^{3+} ions into Cd–Zn–S lattice [25]. It is confirmed that lattice constants were seen to increase at slightly increased crystallite sizes. The lattice micro-strain of Bi^{3+} doped $Cd_{0.9-x}Zn_{0.1}S$ QDs obtained using the below-given formula [26].

$$\text{Micro} - \text{strain}\ (\varepsilon) = \frac{\beta \cos\theta}{4} \quad (2)$$

It is also observed from the Table 1 that the micro-strain decreases with increasing Bi^{3+} ions concentrations. The obtained micro-strain value was gradually decreased with the increase of Bi^{3+} ions (x = 1–5) as shown in Fig. 2d. The decrease of micro-strain with increasing Bi^{3+} ions due to the decrease in the dislocation density (δ), FWHM and the increase of crystallite size (D). The lattice defects like δ and ε showed a decreasing trend with increasing Bi^{3+} doping concentrations, which may be due to the improvement of

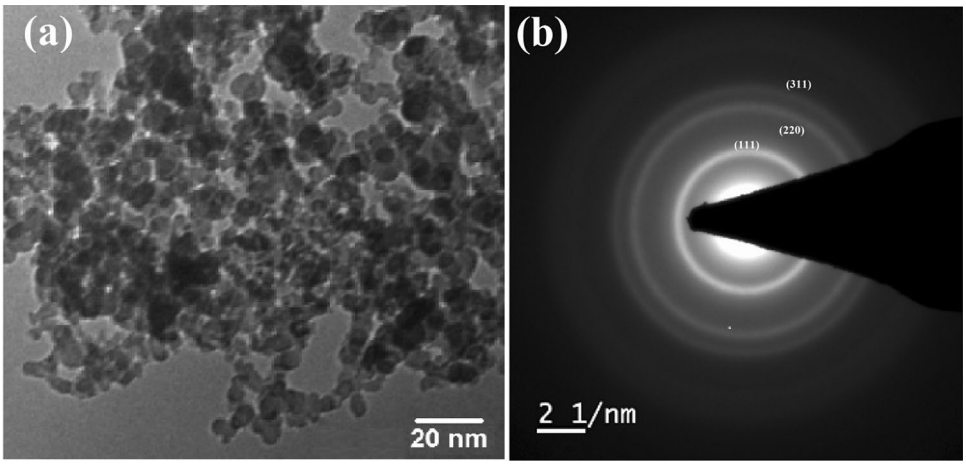

Fig. 3 **a** TEM and **b** SAED photo of $Cd_{0.9-x}Zn_{0.1}S$ QDs

crystalline as well as appropriate orientation along (111) direction.

The TEM picture of Un-doped Zn:CdS QDs was shown in Fig. 3a. We could find spherical-shaped small-sized fine particles. We couldn't find the particles size since the particle are aggregated like a chain. The SAED pattern is given in Fig. 3b. We can view three concentric rings corresponding to (111) (220) (311) plane respectively. The diffraction patterns are in good agreement with XRD results.

3.2 Surface morphological investigations

The surface morphology of $Cd_{0.9-x}Zn_{0.1}Bi_xS$ (x = 0, 0.01, 0.03, 0.05) QDs is examined by Scanning Electron Microscopy. SEM images and their corresponding EDAX spectra of $Cd_{0.9-x}Zn_{0.1}Bi_xS$ QDs with different x values are presented in Fig. 4a–d. The QDs particle size and its distribution mainly depend on relative rates of nucleation of particles and the agglomeration rate. In Fig. 4a pure $Cd_{0.1}Zn_{0.9}S$ QDs reveal lamellar and agglomerate microstructure features. Agglomerated structures occur during the synthesis process and local strain in the nanocrystal, its results in non-homogenous nanoparticles are distributed inside the sample [27]. Figure 4b shows the microstructure of $Cd_{0.89}Zn_{0.1}Bi_{0.01}S$ QDs (x = 0.01); the image observed an almost uniform spherical shape. Moreover, it shows the large cluster of particles having smaller dimensions and also the occurrence of voids can be observed on the surface. Figure 4c presents $Cd_{0.87}Zn_{0.1}Bi_{0.03}S$ QDs (x = 0.03); it can be seen that the QDs particles have a good interfacial bond formed between $Cd_{0.1}Zn_{0.9}S$ and Bi^{3+} ions. Furthermore, it clearly shows a surface topography morphological change in the microstructures of the sample. Figure 4d microstructure of $Cd_{0.85}Zn_{0.1}Bi_{0.05}S$ QDs (x = 0.05), which is similar to Fig. 4b but average particle sizes are increased. It's indicating that Bi^{3+} doping is efficiently inhibited on the surface of $Cd_{0.1}Zn_{0.9}S$ QDs [28]. The undoped and Bi^{3+} ions doped $Cd_{0.1}Zn_{0.9}S$ QDs sample was further confirmed by EDAX analysis as shown on the right-hand side of Fig. 4a–d. This shows that the pure $Cd_{0.1}Zn_{0.9}S$ QDs contain the cadmium (Cd), zinc (Zn) and sulfur (S) elements whereas the doped samples contain the Cd, Zn, S and bismuth (Bi) elements as expected. All the elements present as per the stoichiometry ratio and it confirmed the doping with the various compositions of Bi^{3+} on $Cd_{0.85}Zn_{0.1}Bi_{0.05}S$ QDs. Thus elemental composition analysis confirms nearly the nominal composition of the prepared samples.

3.3 Optical properties analysis of $Cd_{0.9-x}Zn_{0.1}Bi_xS$ QDs

3.3.1 UV–vis absorption analysis

Figure 5a shows the UV–vis absorption spectra of $Cd_{0.9-x}Zn_{0.1}Bi_xS$ QDs (x = 0, 0.01, 0.03 and 0.05) with recorded in the wavelength range of 300–600 nm. All the prepared samples show a very strong and steep absorption edge due to light scattering at a high concentration of the QDs. While the steep edge indicates that the UV–vis light absorption due to the transition from impurity levels formed by Bi^{3+} doped into $Cd_{0.9-x}Zn_{0.1}S$ QDs. It can be seen that high absorption intensity at an electromagnetic wavelength range of $\lambda < 350$ nm, and it is rapidly decreased in the wavelength range of 300 nm $\leq \lambda \leq$ 350 nm. When the wavelength is greater than 350 nm, the absorption value is very small. As Bi^{3+} ions increases notable increase absorption intensity and absorption edge shifting towards lower wavelength ($\lambda x = 1, \lambda x = 3, \lambda x = 5 < \lambda x = 0 \sim 340$ nm, i.e., blue shift) side is due to quantum size effect and alloy composition formation and this phenomenon is well-known Burstein–Moss effect that denotes blue shift is formed with increasing doping concentrations [29, 30]. And also this shift related to band edge indicates that the band gap of the light in response and it can be controlled with Cd^{2+}: Bi^{3+} ratio in $Cd_{0.9-x}Zn_{0.1}Bi_xS$ QDs. The prepared QDs

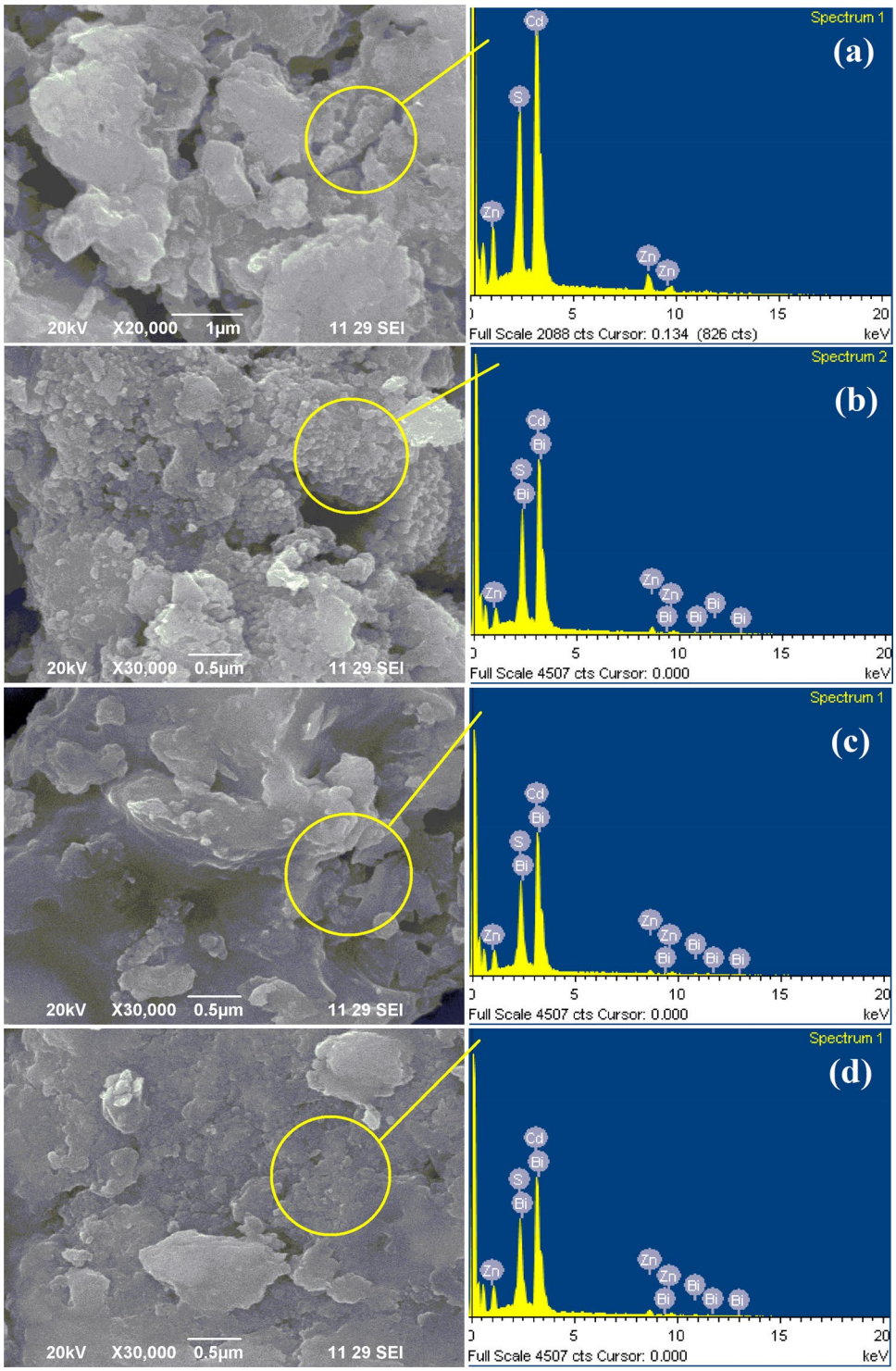

Fig. 4 SEM and EDAX images of $Cd_{0.9-x}Zn_{0.1}Bi_xS$ QDs with differentBi^{3+} ion concentrations

exhibited escalate light absorption intensity than pure $Cd_{0.9-x}Zn_{0.1}S$ in the UV region. The reduced transmittance peak in the UV–vis region is caused by the Bi^{3+} ions increasing the localized state density of sulfur vacancies. The transmission loss is due to light scattering at centers of the $Cd_{0.9-x}Zn_{0.1}Bi_xS$ QDs. The decrease in optical transmission may be associated with the loss of light due to sulfur vacancies.

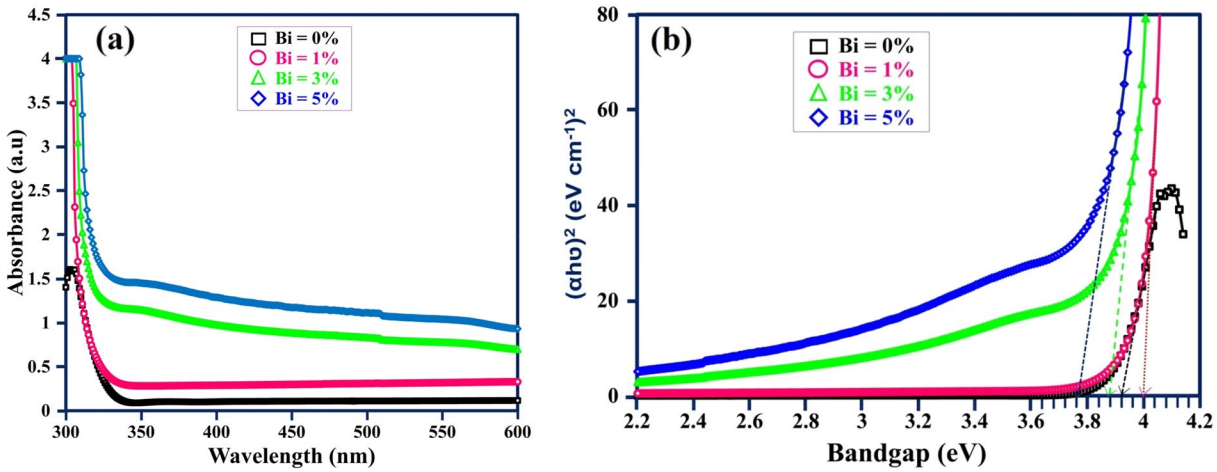

Fig. 5 **a** UV–vis absorption spectra of $Cd_{0.9-x}Zn_{0.1}Bi_xS$ QDs with different Bi^{3+} ion concentrations, **b** The $(\alpha h\upsilon)^2$ versus hυ curves of $Cd_{0.9-x}Zn_{0.1}Bi_xS$ QDs for the optical band gap calculation

3.3.2 Optical energy band gap (E_g)

The optical energy band gap (E_g) of $Cd_{0.9-x}Zn_{0.1}Bi_xS$ QDs ($0 \le x \le 0.05$) is derived from Tauc relation by analyzing optical absorption data. This expression is related to the absorption coefficient as a function of incident photon energy [31].

$$(\alpha h\nu) = A(h\nu - E_g)^n \tag{3}$$

where α is the absorption coefficient, h is a Planck constant (6.626×10^{-34} m^2kg/s), $h\upsilon$ refers to the incident photon energy, A is a constant, E_g is the band gap energy and n is a constant. The optical absorption index (n) value depends on the type of transition and it is equal to 0.5, 1.5, 3 respectively for direct allowed, direct forbidden, indirect allowed or indirect forbidden transition. Here it takes a direct allowed transition, Hence the n value was taken as 0.5. The extrapolating straight lines of the graph $(\alpha h\upsilon)^2$ vs (hυ) to intercept at photon energy x-axis ($\alpha = 0$) gives the value of the energy band gap (Eg) shown in Fig. 5b. It has been shown that pure $Cd_{0.9-x}Zn_{0.1}S$ QDs have E_g value equal to 3.92 eV which is slightly higher than 3.8 eV reported in the literature [32]. The higher E_g (4 eV) value was observed for $x = 0.01$, which may due to the size effect. Generally, The quantum confinement effect influences the blue shift of band gap. But in the present case size effect dominates the quantum confinement effect, because the particle size was increased due to the incorporation of dopant. On the other hand, the larger band gap of Bi^{3+} ions initially produces many donor levels in the $Cd_{0.9-x}Zn_{0.1}Bi_xS$ QDs. Hence the Fermi energy (EF) level is shifted more away from the valence band and increases the E_g value. With a further increase in the doping concentration, the E_g value slightly decreased (redshift) as a function of Bi^{3+} ion concentration. The blue shift is blocking off the QDs mainly arises from the low energy transitions in optical band-to-band transitions. The observed decreased energy gap values are $E_g = 3.88$ eV and 3.76 eV corresponding to $x = 0.03$ and 0.05. The decrease of the energy gap is due to Bi^{3+} ions, which increases the internal pressure because Bi^{3+} ion has a larger ionic size than Cd^{2+} and also due to the presence of layered morphology with lower carrier density [33].

3.4 FT-IR functional group analysis of $Cd_{0.9-x}Zn_{0.1}Bi_xS$ QDs

Figure 6 shows the FT-IR spectra of undoped and Bi^{3+} ions doped $Cd_{0.9-x}$ $Zn_{0.1}Bi_xS$ QDs ($0 \le x \le 0.05$) were recorded in the wavelength range of 400–4000 cm^{-1}. The data are presented in the table, from which the peak around 3338–3401 cm^{-1} is attributed to the O–H stretching vibrating mode of the water molecule. It's indicating that the presence of H_2O molecules on the surface of $Cd_{0.9-x}Zn_{0.1}Bi_xS$ QDs. A very weak band corresponds to inter H-bonding is observed at 2923–3008 cm^{-1}. The peaks at 2346–2375 cm^{-1} were due to the presence of CO_2 in the sample. The major absorption peak at 1566–1633 cm^{-1} attributed to H–O–H stretching vibration mode [34]. The strong absorption peaks centered at 1405, 1410 and 1411 cm^{-1} are ascribed to the C–H bending vibration mode. The presence of characteristic peaks at 108–1020 cm^{-1} and 147–148 cm^{-1} corresponding to the symmetric and asymmetric form of the C–O stretching vibration band. The weak absorption peak at 830 cm^{-1} is due to Cd–S stretching vibration frequency. The narrow absorption peaks around 620 and 670 cm^{-1} are assigned to Zn–S vibration due to the stretching mode of Cd–Zn–S

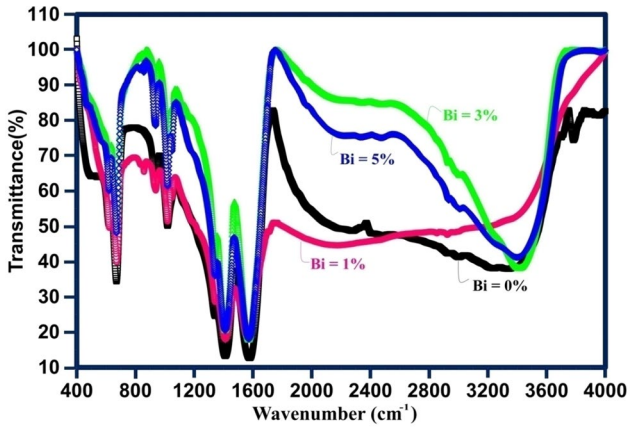

Fig. 6 FTIR spectra of $Cd_{0.9-x}Zn_{0.1}Bi_xS$ QDs with different Bi concentrations from 0 to 5% in the wave number from 400 to 4000 cm^{-1}

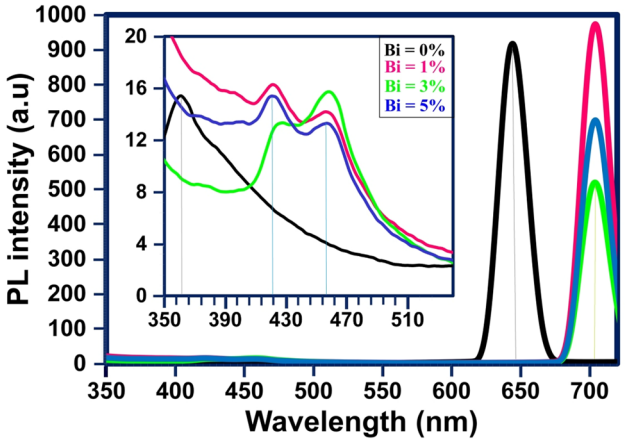

Fig. 7 PL spectra of $Cd_{0.9-x}Zn_{0.1}Bi_xS$ QDs with respect to Bi^{3+}concentrations (x = 0, 1, 3 and 5)

[35]. The IR peaks assigned for various vibrations are given in Table 2.

3.5 Photoluminescence properties of $Cd_{0.9-x}Zn_{0.1}Bi_xS$ QDs

The room temperature photoluminescence spectra of $Cd_{0.9-x}Zn_{0.1}Bi_xS$ QDs with different Bi^{3+} compositions (x = 0, 1, 3 and 5) are illustrated in Fig. 7. The measurement was performed wavelength range is 350–750 nm with excitation wavelength 350 nm. From the PL spectrum, it was observed that five intensity fluorescence emission bands, three weak peaks are on the lower wavelength side and two strong emission peaks are on the higher wavelength side. That emission bands are near ~ 365, ~ 422, ~ 454, ~ 648 and ~ 712 nm corresponding to Bi^{3+} doped $Cd_{0.9-x}Zn_{0.1}S$ QDs. The PL1 band corresponding to the undoped $Cd_{0.9}Zn_{0.1}S$ QDs sample, which exhibits a broad emission peak centered at ~ 365 nm in the ultraviolet luminescence region.

This near band edge emission (NBE) is generally attributed to the recombination of free excitons (e^- h^+) present in the $Cd_{0.9}Zn_{0.1}S$ QDs lattices and also due to the transition of an electron trapped in the sulfur vacancy to the valence band. This UV emission peak (~ 365 nm) intensity is suitable for the treatment of psoriatic and skin diseases. The Bi^{3+} doped $Cd_{0.9}Zn_{0.1}S$ sample shows that the next two broad excitation bands between 420 and 470 nm, which peak centered at ~ 422 nm and ~ 456 nm. These peaks are ascertained to the localized energy level introduced by Bi^{3+} dopant ion, which acts as an acceptor impurity and the emission arises from the sulfur vacancy to the Bi^{3+} dopant level. This violet-blue emission peak ~ 422 nm originates from the transition of the shallow trap level (STL) [36]. The peak centered at ~ 456 nm may be attributed to a higher level of excitonic emission caused by the size effect. The intensity of blue color emission band at 456 nm becomes high toward the higher Bi^{3+} doping concentration (x = 5) and there is no excitation peaks are observed at 422 nm and 456 nm corresponding x = 0. The photoluminescence properties of these structures are investigated aiming at the field of blue and violet-blue light-emitting diodes (LEDs) [37].

Table 2 IR peaks and their assignments of $Cd_{0.9-x}Zn_{0.1}Bi_xS$ QDs (x = 0% to 5%) at room temperature

Assignments	Wave number (cm^{-1})			
	$Cd_{0.9}Zn_{0.1}S$	$Cd_{0.89}Zn_{0.1}Bi_{0.01}S$	$Cd_{0.87}Zn_{0.1}Bi_{0.03}S$	$Cd_{0.85}Zn_{0.1}Bi_{0.05}S$
O–H stretching vibration of H_2O	3338	3401	3341	3399
C=O stretching vibration due CO_2	2375	–	–	2346
H–O–H bending vibration of H_2O	1621	1566	1571	1573
C–H bending vibration	1405	1411	1410	1410
C–O asymmetric stretching bonds	1018	1018	1020	1018
Stretching mode of Cd–Zn–S (doublet)	619 670	620 671	620 671	620 671

On a longer wavelength side (λ ≥ 600 nm) a defect related to deep-level emission (DLE) was produced. It was observed that the photoluminescence (PL) emission from the $Cd_{0.9}Zn_{0.1}S$ QDs can be easily tuned from the red (648 nm) to deep red (712 nm) region of visible light by adding Bi^{3+} doping concentration (x = 1, 3 and 5) into $Cd_{0.9}Zn_{0.1}S$ QDs [38]. This strong and narrow emission peak may be due to band to band transition. It can be seen that the PL emission spectra of all samples, the Gaussian shape did not change significantly except for the PL emission intensity. Not change in Gaussian shape due to the end of chemical reaction to stabilize the synthesized nanocrystals. Moreover, the PL spectra of $Cd_{0.9}Zn_{0.1}S$: Bi^{3+}sample show a strong emission at x = 1 corresponding wavelength is 712 nm. Further adding Bi^{3+} doping into the $Cd_{0.9}$ $Zn_{0.1}S$ sample the peak slightly shifted towards a longer wavelength (Red-shift ~ 1.75 nm) side and emission intensity decreased due to the quenching phenomenon [39]. This small red shift in PL peak was confirmed from XRD. The PL peak decreased with the increase of Bi^{3+} doping amount, indicating that the recombination of photo-generated electron–hole pairs in bulk crystal defects was efficiently depressed. This observed change in the PL emission wavelength can be highly beneficial the imaging screen applications [40].

3.6 Electrochemical study

Cyclic Voltammetry (CV) is a primary method to study the developed current in an electrochemical cell under the voltage that goes beyond the anticipated value by the Nernst equation. Figure 8 shows the cyclic voltammograms of Bi^{3+}-doped $Cd_{0.9}Zn_{0.1}S$ QDs. The cathodic current density (J_{pc}) and anodic current density (J_{pa}) are taken for the present investigation in this study. The high (J_{pc}) current peak value was obtained for Bi = 0% incorporated into

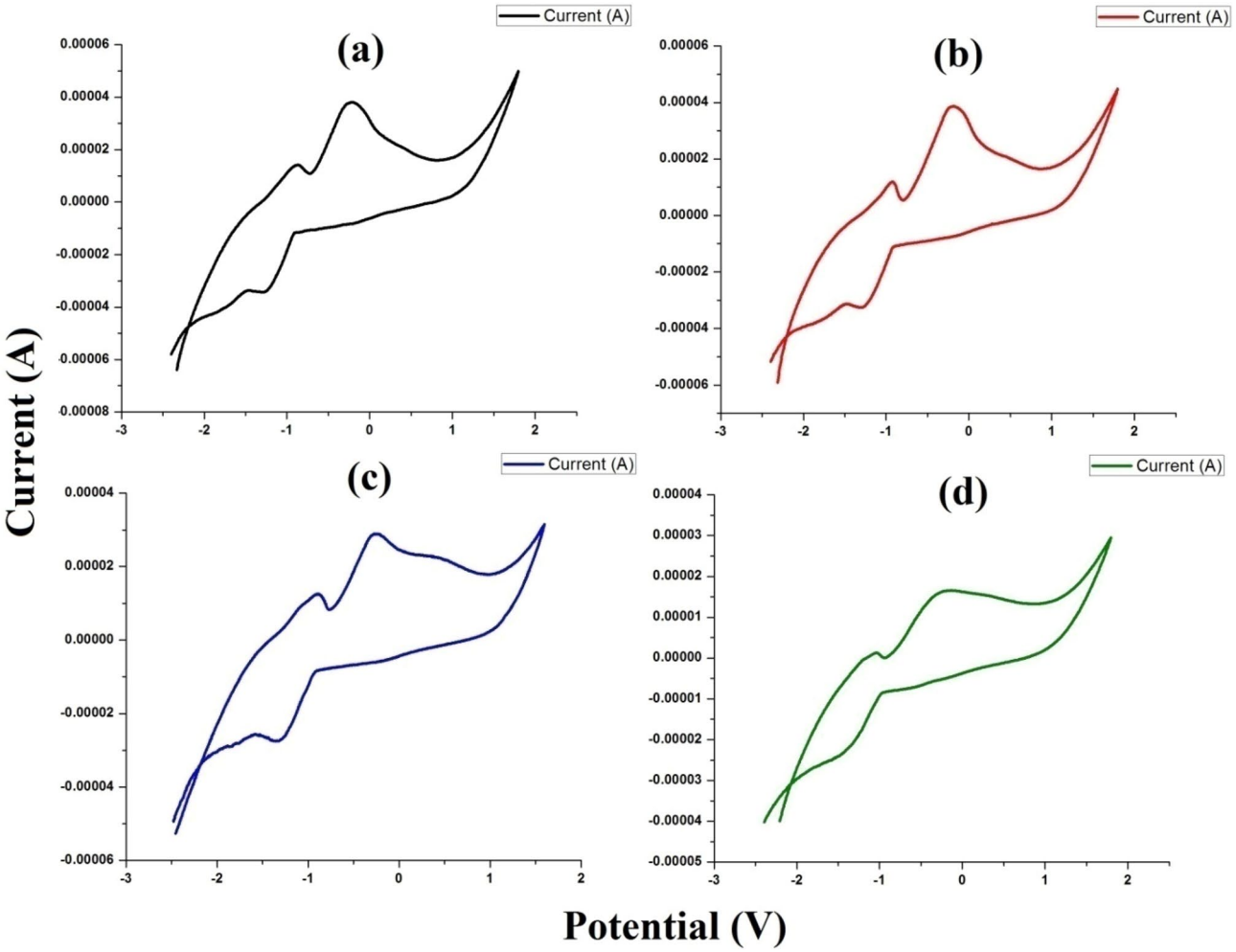

Fig. 8 CV analysis of $Cd_{0.9-x}Zn_{0.1}Bi_xS$ QDs

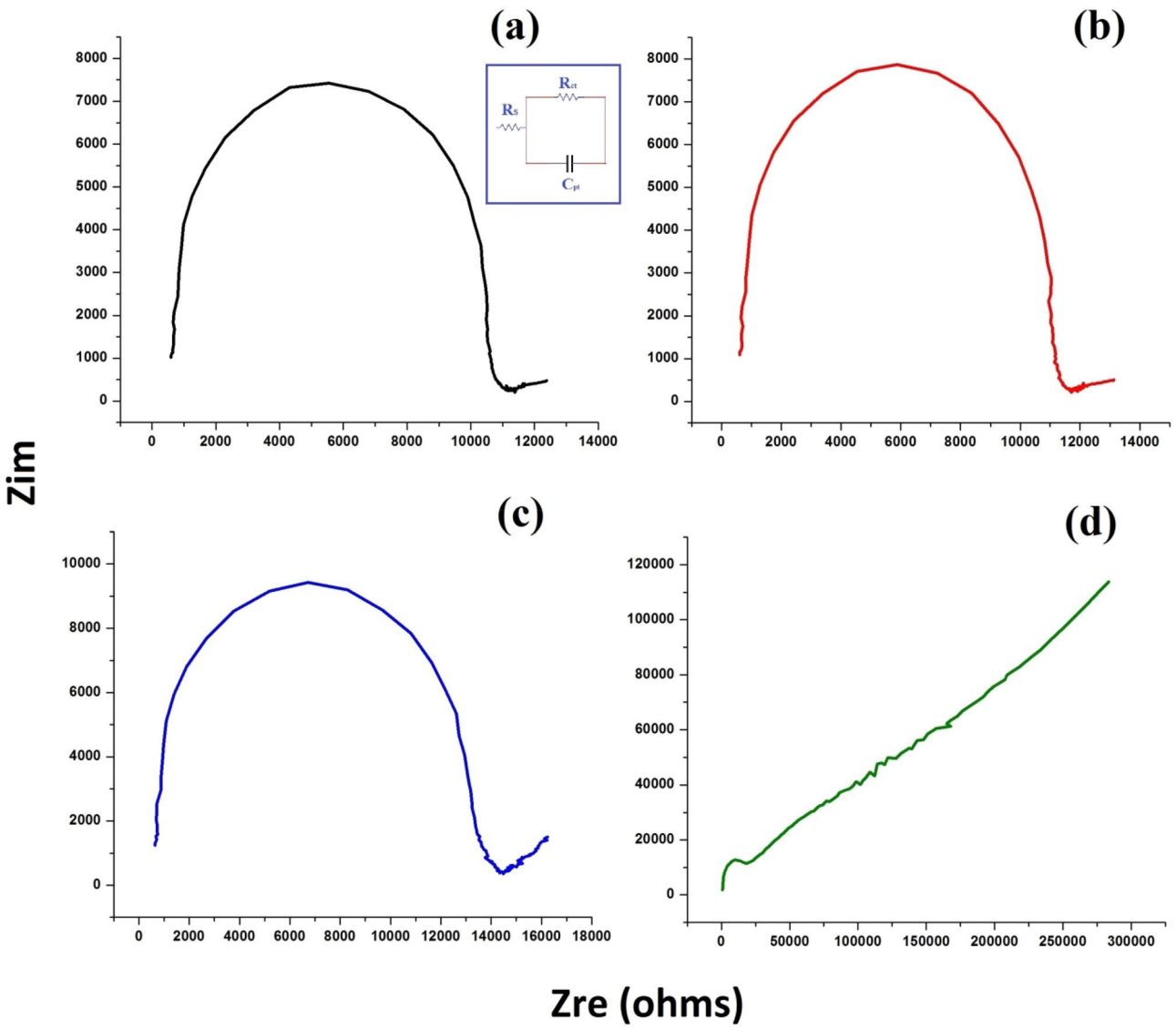

Fig. 9 Nyquist plot for $Cd_{0.9-x}Zn_{0.1}Bi_xS$ QDs

$Cd_{0.9}Zn_{0.1}S$ QDs. The high value of peaks observed either in positive and negative current values for Bi = 0%. ΔE_P is referred to as peak to peak separation value. The value of ΔE_P is calculated by the given relation [41]

$$\Delta E_P = E_{pc} - E_{pa} \tag{4}$$

The crystallite nature of the materials with low resistivity indicates the fast charge transfer kinetics**.** The low ΔE_P values deduced an enhanced catalytic activity [42].

The Nyquist plots were plotted for the samples used in this work and they were depicted in Fig. 9. From the analysis, the maximum diameter value of the semicircle was observed for Bi^{3+} = 5% and it was further moved towards a very high-frequency side. The semi-circle area of Bi = 5% was increased than the other compositions of Bi. The semi-circle reaches a higher percentage for Bi^{3+} = 5%. The R_{ct} represents the charge transfer resistance for the semi-circle on the higher frequency side. Where, R_S is denoted as series resistance for the intercept on the real axis near the higher frequency side [43]. The proposed equivalent circuit for these elements is shown in Fig. 9. From the figure, the R_s and R_{ct} values of Bi^{3+} = 0% doped $Cd_{0.9}Zn_{0.1}S$ QDs very lower than the other compositions. As low resistance was exhibited by Bi^{3+} = 0% doped $Cd_{0.9}Zn_{0.1}S$ QDs, this combination offered an excellent electrical feature.

4 Conclusion

The $Cd_{0.9-x}Zn_{0.1}Bi_xS$ QDs have been synthesized by a controlled co-precipitation method at room temperature with different (x = 0, 0.01, 0.03, 0.05) values. XRD studies revealed that the samples had a cubic structure and the average crystallite size was varied from 2.13 nm to 5.98 nm for the various doping concentration of Bi^{3+} ions. SEM images showed that the surface morphology of the prepared QDs possessed agglomerate microstructure and morphology modified from unequally sized grains to nearly equally sized grains with the increase of dopant concentration. The elemental analysis (EDAX) and FT-IR studies confirmed the presence of elements as they are expected. The UV–vis absorption intensity increased with the increase of Bi^{3+} concentration. High absorption intensity (lab) was observed in the wavelength range 300 nm ≤ λ ≤ 350 nm. Optical band gap (Eg) values of doped CdS QDs were different from the bulk CdS nanocrystal. The Eg value of $Cd_{0.9-x}Zn_{0.1}Bi_xS$ QDs could be tailored from 3.76 to 4 eV by varying the doping ratio of Bi^{3+} ions. Bi^{3+}-doped $Cd_{0.9}Zn_{0.1}S$, the emission intensity was maximum for 1% doping. The PL emission for $Cd_{0.9-x}Zn_{0.1}Bi_xS$ QDs have been received in violet, blue and red colour regions and the emission peak position was shifted to higher wavelength side due to the incorporation of Bi^{3+} ions. The incorporation of Bi^{3+} ions increases the electrical resistivity of Zn:CdS QDs. As Bi^{3+}-doped Zn:CdS QDs exhibited excellent optical and photoluminescence properties the doping ratio of Bi^{3+} (1%), this combination shall be selected for the fabrication of red-emitting diodes, labelling and imaging applications.

Declartions

Conflict of interest The authors declare that they have no competing interests.

References

1. Chen O, Wei H, Maurice A, Bawendi M, Reiss P (2013) Pure colors from core–shell quantum dots. MRS Bull 38:696–702. https://doi.org/10.1557/mrs.2013.179
2. Yu WW, Chang E, Drezek R, Colvin VL (2006) Water-soluble quantum dots for biomedical applications. Biochem Biophys Res Commun 348:781–786. https://doi.org/10.1016/j.bbrc.2006.07.160
3. Rahman MM, Karim MR, Alam MM, Zaman MB, Alharthi N, Alharbi H, Asiri AM (2020) Facile and efficient 3-chlorophenol sensor development based on photolumenescent core-shell CdSe/ZnS quantum dots. Sci Rep 10:557. https://doi.org/10.1038/s41598-019-57091-6
4. Murphy CJ (2002) Optical sensing with quantum dots anal. Chem 74:520A-526A. https://doi.org/10.1021/ac022124v
5. Khan AH, Bertrand GHV, Teitelboim A, Chandra Sekhar M, Polovitsyn A, Brescia R, Planelles J, Climente JI, Oron D, Moreels I (2020) CdSe/CdS/CdTe Core/Barrier/Crown nanoplatelets: synthesis, optoelectronic properties, and multiphoton fluorescence upconversion. ACS Nano 14:4206–4215. https://doi.org/10.1021/acsnano.9b09147
6. Liang J, Devakumar B, Sun L, Wang S, Sun Q, Guo H, Huang X (2019) Deep-red-emitting $Ca_2LuSbO_6:Mn^{4+}$ phosphors for plant growth LEDs: Synthesis, crystal structure, and photoluminescence properties. J Alloys Compd 804:521–526. https://doi.org/10.1016/j.jallcom.2019.06.312
7. Zhang L, Che W, Yang Z, Liu X, Liu S, Xie Z, Zhu D, Su Z, Tang BZ, Bryce MR (2020) Bright red aggregation-induced emission nanoparticles for multifunctional applications in cancer therapy. Chem Sci 11:2369–2374. https://doi.org/10.1039/C9SC06310B
8. Zhou Y, Zhang L, Gao W, Yang M, Lu J, Zheng Z, Zhao Y, Yao J, Li J (2021) A reasonably designed 2D WS2 and CdS microwire heterojunction for high performance photoresponse. Nanoscale 13:5660–5669. https://doi.org/10.1039/D1NR00210D
9. Ananthakumar S, Balaji D, Ramkumar J (2019) Role of co-sensitization in dye-sensitized and quantum dot-sensitized solar cells. SN Appl Sci 1:186. https://doi.org/10.1007/s42452-018-0054-3
10. Wang Y, Chen V, Liu L, Xi X, Li Y, Geng V, Jiang G, Zhao Z (2019) Novel metal doped carbon quantum dots/CdS composites for efficient photocatalytic hydrogen evolution. Nanoscale 11:1618–1625. https://doi.org/10.1039/C8NR05807E
11. Dzhagan VM, Stroyuk OL, Rayeveska OE, Kuchmiy SY, Valakh MY, Azhniuk YM, Borczyskowski CV, Zahn DRT (2010) A spectroscopic and photochemical study of Ag^+-, Cu^{2+}-, Hg^{2+}-, and Bi^{3+}-doped $Cd_xZn_{1-x}S$ nanoparticles. J Colloid Interface Sci 345:515–523. https://doi.org/10.1016/j.jcis.2010.02.001
12. Zhang G, Chen D, Li N, Xu Q, Li H, He J, Lu, (2019) Fabrication of Bi_2MoO_6/ZnO hierarchical heterostructures with enhanced visible-light photocatalytic activity, J Appl. Catal B 250:313–324. https://doi.org/10.1016/j.apcatb.2019.03.055
13. Krishnamoorthy A, Sakthivel P, Devadoss I, Illayaraja Muthaiya VM (2020) Structural, morphological and photoluminescence characteristics of $Cd_{0.9-x}Zn_{0.1}S$ quantum dots: Effect of Fe2+ ion. Optik. https://doi.org/10.1016/j.ijleo.2020.164220
14. Kavi Rasu K, Sakthivel P, Prasanna Venkatesan GKD (2020) Effect of Pd^{2+} co-doping on the structural and optical properties of Mn^{2+}:ZnS nanoparticles. Opt Laser Technol 130:106365. https://doi.org/10.1016/j.optlastec.2020.106365
15. Sirajunisha H, Sakthivel P, Balakrishnan T (2021) Structural, photoluminescence, antibacterial and biocompatibility features of zinc incorporated hydroxyapatite nanocomposites. J Mater Sci: Mater Electron 32:5050–5064. https://doi.org/10.1007/s10854-021-05239-4

16. Tzanidis I, Bairamis F, Sygellou L, Andrikopoulos KS, Avgeropoulos A, Konstantinou L, Tasis D (2020) Rapid microwave-assisted synthesis of CdS/Graphene/MoSx tunable heterojunctions and their application in photocatalysis. Chem Eur J 26:6643. https://doi.org/10.1002/chem.202000131
17. Li S, Wang P, Zhao H, Wang R, Jing R, Meng Z, Li W, Zhang Z, Liu Y, Zhang Q, Li Z (2021) Fabrication of black phosphorus nanosheets/BiOBr visible light photocatalysts via the co-precipitation method. Colloids Surf A Physicochem Eng Asp 612:125967. https://doi.org/10.1016/j.colsurfa.2020.125967
18. Mariappan R, Ponnuswamy V, Ragavendar M, Krishnamoorthi D, Sankar C (2012) The effect of annealing temperature on structural and optical properties of undoped and Cu doped CdS thin films. Optik 123:1098–1102. https://doi.org/10.1016/j.ijleo.2011.07.038
19. Anjum S, Sehar F, Awan MS, Zia R (2016) Role of Bi^{3+} substitution on structural, magnetic and optical properties of cobalt spinel ferrite. Appl Phys A 122:436. https://doi.org/10.1007/s00339-016-9798-z
20. Devadoss I, Sakthivel P (2020) Effect of Mg on $Cd_{0.9}$–x$Zn_{0.1}S$ nanoparticles for optoelectronic applications. J Appl Phys A. 126:315. https://doi.org/10.1007/s00339-020-03490-w
21. Muhammed Shafi P, Chandra Bose A (2015) Impact of crystalline defects and size on X-ray line broadening: a phenomenological approach for tetragonal SnO_2 nanocrystals. AIP Adv 5:057137. https://doi.org/10.1063/1.4921452
22. Kazmi J, Ooi PC, Goh BT, Lee MK, Wee MFMR, Karim SSA, Raza SRA, Mohamed MA (2020) Bi-doping improves the magnetic properties of zinc oxide nanowires. RSC Adv 10:23297. https://doi.org/10.1039/d0ra03816d
23. Wang W, Lee GJ, Wang P, Qiao Z, Liu N, Wu JJ (2020) Microwave synthesis of metal-doped ZnS photocatalysts and applications on degrading 4-chlorophenol using heterogeneous photocatalytic ozonation process. Sep Purif Technol 237:116469. https://doi.org/10.1016/j.seppur.2019.116469
24. Mahmood W, Shah NA (2014) CdZnS thin films sublimated by closed space using mechanical mixing: a new approach. Opt Mater 36:1449. https://doi.org/10.1016/j.optmat.2013.09.003
25. Azizi S, Dizaji HR, Ehsani MH (2016) Structural and optical properties of Cd1-xZnxS (x = 0, 0.4, 0.8 and 1) thin films prepared using the precursor obtained from microwave irradiation processes. Optik 127:7104–7114. https://doi.org/10.1016/j.ijleo.2016.05.030
26. Sakthivel P, Kavirasu K, Prasanna Venkataesan GKD, Viloria A (2020) Influence of Ag^{+} and Mn^{2+} ions on structural, optical and photoluminescence features of ZnS quantum dots. Spectrochim Acta, Part A 241:118666. https://doi.org/10.1016/j.saa.2020.118666
27. Bakhsh A, Gul IH, Maqood A, Wu SH, Chan CH, Chang YC (2016) Size dependent photoluminescence properties of CdZnS nanostructures. J Lumin 179:574–580. https://doi.org/10.1016/j.jlumin.2016.07.065
28. Selvan G, Abubacker MP, Balu AR (2016) Structural, optical and electrical properties of Cl-doped ternary CdZnS thin films towards optoelectronic applications. Optik 127:4943–4947. https://doi.org/10.1016/j.ijleo.2016.02.047
29. Heiba ZK, Bakr M, Imam NG (2015) Hybrid luminescent CdS@ZnS nanocomposites ceram. Int 41:12930–12938. https://doi.org/10.1016/j.ceramint.2015.06.135
30. Klyuev VG, Volykhin DV, Smirnov MS, Dubovitskaya NS (2017) Influence of manganese doping on the luminescence characteristics of colloidal $Zn_xCd_{1-x}S$ quantum dots in gelatin. J Lumin 19:893–901
31. Kumar R, Sakthivel P, Mani P (2019) Structural, optical, electrochemical, and antibacterial features of ZnS nanoparticles: incorporation of Sn. Appl Phys A 125:543. https://doi.org/10.1007/s00339-019-2823-2
32. Sakthivel P, Prasanna Venkatesan GKD, Subramaniam K, Muthukrishnan P (2019) Structural, optical, photoluminescence and electrochemical behaviours of Mg Mn dual-doped ZnS quantum dots. Mater Sci: Mater Electron 30:11984–11993
33. Devadoss I, Sakthivel P, Pauline Sheeba S (2021) Influence of Sn^{2+} ion on structural, morphological and optical characteristics of $Cd_{0.9-x}Zn_{0.1}Sn_xS$ ($0 \le x \le 0.06$) quantum dots. Indian J Phys 95:741–747. https://doi.org/10.1007/s12648-020-01735-1
34. Yellaiah G, Hadasa K, Nagabhushanam M (2013) Structural, optical and vibrational studies of Na^{+} doped $Cd_{0.8}Zn_{0.2}S$ semiconductor compounds. J Alloys Compd 581:805–811. https://doi.org/10.1016/j.jallcom.2013.07.191
35. Prajapati B, Kumar S, Kumar M, Chatterjee S, Ghosh AK (2017) Investigation of the physical properties of Fe:TiO_2-diluted magnetic semiconductor nanoparticles. J Mater Chem C 5:4257–4267. https://doi.org/10.1039/C7TC00233E
36. Wang CQ, Xiab JX, Ali MU, Liu M, Lu W, Meng H (2019) Facile synthesis of enhanced photoluminescent Mg:CdZnS/Mg:ZnS core/shell quantum dots. Mater Sci Semicond Process 92:96–102. https://doi.org/10.1016/j.mssp.2018.07.007
37. Liang H, Wang Z, Wang J, Huang D, Zhu Y, Song Y (2017) Synthesis of Fe(1–x)Znx@Zn(1-y)FeyOz nanocrystals via a simple programmed microfluidic process. Mater Chem Phys 201:156–164. https://doi.org/10.1016/j.matchemphys.2017.08.005
38. Zhang K, Zhou Z, Guo L (2011) Alkaline earth metal as a novel dopant for chalcogenide solid solution: Improvement of photocatalytic efficiency of $Cd_{1-x}Zn_xS$ by barium surface doping. Int J Hydrogen Energy 36:9469–9478. https://doi.org/10.1016/j.ijhydene.2011.05.058
39. Sakthivel P, Muthukumaran S (2017) Investigation of Ni influence on structural and band gap tuning of $Zn_{0.98}Mn_{0.02}S$ quantum dots by co-precipitation method. J Mater Sci: Mater Electron 28:8309–8315. https://doi.org/10.1007/s10854-017-6545-y
40. Lettieri S, Setaro A, Baratto C, Comini E, Faglia G, Sberveglieri G, Maddalena P (2008) On the mechanism of photoluminescence quenching in tin dioxide nanowires by NO2 adsorption. New Phys 10:043013. https://doi.org/10.1088/1367-2630/10/4/043013
41. Faulkner S, Pope SJA, Pye BPB (2005) Lanthanide complexes for luminescence imaging applications. Appl Spectrosc Rev 40:1. https://doi.org/10.1081/ASR-200038308
42. Ma J, Shen W, Li C, Yu F (2018) Light reharvesting and enhanced efficiency of dye-sensitized solar cells based 3D-CNT/graphene counter electrodes. J Mater Chem A 3:12307–12313. https://doi.org/10.1039/C5TA02214B
43. Swami SK, Chaturvedi N, Kumar A, Chander N, Dutta V, Kumar DK, Ivaturi A, Senthilarasu S, Upadhyaya HM (2014) Spray deposited copper zinc tin sulphide (Cu_2ZnSnS_4) film as a counter electrode in dye sensitized solar cells. PhysChemChemPhys 16:23993–23999. https://doi.org/10.1039/C4CP03312D